

Unidirectional Ray Polaritons in Twisted Asymmetric Stacks

J. Álvarez-Cuervo^{1,2*}, M. Obst^{3,4*}, S. Dixit^{5,*}, G. Carini⁶, A. I. F. Tresguerres-Mata^{1,2}, C. Lanza^{1,2}, E. Terán-García^{1,2}, G. Álvarez-Pérez^{1,2,6,7}, L. Fernández-Álvarez^{1,2}, K. Diaz-Granados⁵, R. Kowalski⁵, A. S. Senerath⁵, N. S. Mueller⁶, L. Herrer⁸, J.M. De Teresa⁸, S. Wasserroth⁶, J. M. Klopff⁹, T. Beechem¹⁰, M. Wolf⁶, L.M. Eng^{3,4}, T.G. Folland¹¹, A. Tarazaga Martín-Luengo^{1,2}, J. Martín-Sánchez^{1,2}, S.C. Kehr^{3,4,†}, A.Y. Nikitin^{12,13,†}, J.D. Caldwell^{5,†}, P. Alonso-González^{1,2,†}, A. Paarmann^{6,†}

¹Department of Physics, University of Oviedo, Oviedo 33006, Spain.

²Center of Research on Nanomaterials and Nanotechnology (CINN), CSIC-Universidad de Oviedo, El Entrego 33940, Spain.

³Institute of Applied Physics, TUD Dresden University of Technology, Dresden, Germany.

⁴Würzburg-Dresden Cluster of Excellence - EXC 2147 (ct.qmat), Dresden 01062, Germany

⁵Vanderbilt University, Nashville, TN, USA.

⁶Fritz Haber Institute of the Max Planck Society, Berlin, Germany.

⁷Center for Biomolecular Nanotechnologies, Istituto Italiano di Tecnologia, Via Barsanti 14, Arnesano, 73010, Italy

⁸Instituto de Nanociencia y Materiales de Aragón (INMA), CSIC-Universidad de Zaragoza, Zaragoza 50009, Spain.

⁹Institute of Radiation Physics, Helmholtz-Zentrum Dresden-Rossendorf, Dresden, Germany.

¹⁰Purdue University and Birck Nanotechnology Center, West Lafayette, IN, USA.

¹¹University of Iowa, Iowa City, IA, USA.

¹²Donostia International Physics Center (DIPC), Donostia-San Sebastián 20018, Spain.

¹³IKERBASQUE, Basque Foundation for Science, Bilbao 48013, Spain.

†Correspondence to:

susanne.kehr@tu-dresden.de, alexey@dipc.org, josh.caldwell@vanderbilt.edu, pabloalonso@uniovi.es, alexander.paarmann@fhi-berlin.mpg.de

*These authors contributed equally to this work

Abstract

The emergence of a vast repository of van der Waals (vdW) materials supporting polaritons – light coupled to matter excitations – offers a plethora of different possibilities to tailor electromagnetic waves at the subwavelength-scale. In particular, the development of twistoptics – the study of the optical properties of twisted stacks of vdW materials – allows the directional propagation of phonon polaritons (PhPs) along a single spatial direction, which has been coined as canalization. Here we demonstrate a complementary type of nanoscale unidirectional propagation that naturally emerges thanks to twistoptics: unidirectional ray polaritons (URPs). This natural phenomenon arises in two types of twisted hyperbolic stacks: homostructures of α -MoO₃ and heterostructures of α -MoO₃ and β -Ga₂O₃, each with very different thicknesses of its constituents. URPs are characterized by the absence of diffraction and the presence of a single phase of the propagating field. Importantly, we demonstrate that this ray behavior can be tuned by means of both relative twist angle and illumination frequency variations. Additionally, an unprecedented “pinwheel-like” propagation emerges at specific twist angles of the homostructure. We show that URPs emerge due to the twist between asymmetrically stacked biaxial slabs, while the shear effect in monoclinic β -Ga₂O₃ is of minor importance. Our findings demonstrate a natural way to excite unidirectional ray PhPs and offer a unique platform for controlling the propagation of PhPs at the nanoscale with many potential applications like nanoimaging, (bio)-sensing or polaritonic thermal management.

In recent years, the exploration of PhPs in polar materials has emerged as a promising avenue in nanophotonics, offering unprecedented control over electromagnetic waves at the nanoscale¹⁻⁴. The applications of PhPs are diverse, encompassing molecule sensors^{5,6}, hyperlensing^{4,7-9}, enhancing thermal emission¹⁰ and detectors¹¹, among others. To engineer nanophotonic devices effectively, it becomes imperative to manipulate the characteristic features of PhPs, such as their wavelength, propagation direction, propagation length or lifetimes. Notably, it has been demonstrated that the fundamental properties of PhPs can be engineered via the choice of the symmetry of the host crystal¹². For instance, while PhPs in uniaxial crystals such as hexagonal boron nitride (hBN) exhibit isotropic in-plane and hyperbolic out-of-plane propagation^{7,8,13,14}, lower symmetry crystals like α -MoO₃ or α -V₂O₅ can support both in- and out-of-plane hyperbolic propagation¹⁵⁻¹⁹, due to their biaxial nature. Typically, the propagation of polaritons for an in-plane hyperbolic media is dominated by the low-momentum components at the base of the hyperbolic Isofrequency Curve (IFC) – a planar cut through the polariton dispersion at a constant frequency¹⁵⁻¹⁹. However, if the propagation is dominated by the asymptotes of the hyperbola, ray-like polaritons emerge along a single spatial direction with a constant phase, which results from the momentum \mathbf{k} being almost entirely perpendicular to the direction of propagation defined by the Poynting vector \mathbf{S} . Besides, these polaritons are highly confined, strongly bound to the interface of the host material, and contain a high density of electromagnetic states²⁰. As a result, ray polaritons can, for example, preserve high resolution, transmitting large- k information over large distances without diffraction²¹, and thus providing a distinctive opportunity for optoelectronic applications that rely on nanoscale waveguiding and steering.

Recent studies have successfully visualized in-plane ray-like polariton modes. For instance, two PhPs rays with a cross-like shape have been observed at the surface of an α -MoO₃ layer placed over a SiC substrate²². A similar effect, but with a pronounced asymmetry between the intensity of the two rays has been demonstrated in crystal off-cuts of calcite^{21,23} and in monoclinic crystals like β -Ga₂O₃ and CdWO₄²⁴⁻²⁷. The asymmetry between these two rays can be so large that effectively only one of the rays is observed. However, in these studies^{21,23-27} the unidirectional ray propagation can only be achieved using specifically designed polariton launchers, or concrete incident polarization conditions that allow for control over which components of the IFCs are excited. Thus, in these systems URPs does not emerge naturally from the materials properties.

The possibility of combining layers of van der Waals (vdW) materials in a single twisted stack expands the potential for engineering and customizing the PhPs dispersion, enabling precise control over their propagation characteristics (known as twistoptics^{12,28-34}). As a hall-mark feature, canalized PhPs – waves propagating along a single spatial direction – have been observed in twisted homostructures of thin α -MoO₃ layers³⁰⁻³⁴. By including a third layer of similar thickness, it is even possible to guide these canalized polaritons along any desirable in-plane direction³⁴. This tunability is crucial to efficiently apply these unidirectional PhPs to a wide range of nanophotonic applications. It is important to note that although both unidirectional ray-like and canalized polaritons propagate along a single spatial direction, defined by a unique direction of the Poynting vector³⁰⁻³⁴, they have clearly distinct propagation behavior: canalized polaritons contain momentum components from many (ideally all) directions of the in-plane momentum space, resulting in periodic amplitude oscillations along the direction of propagation. In contrast, URPs exhibit momentum components only from a single direction perpendicular to the direction of propagation, resulting in a non-oscillatory propagation exhibiting a constant phase.

Here, we report the experimental observation of URPs being naturally supported in twisted asymmetric structures composed of a thin and a thick hyperbolic layer, where the thickness disparity induces a strong symmetry breaking within the system. Remarkably, these URPs exhibit a high degree of tunability through changing either the illumination frequency or the twist angle, i.e. without the need for specific antenna designs or illumination conditions. In particular, we observe URPs in two complementary systems: a twisted homostructure comprising of identical

hyperbolic materials for each layer, and a twisted heterostructure featuring different hyperbolic materials, with strongly asymmetric layer thicknesses in both systems. The emergence of URPs in both homo- and heterostructures demonstrates the versatile nature of the phenomenon, thereby advancing our understanding and broadening the applicability of twist-optical platforms.

Schematics of the two systems are shown in Fig.1a,b. A thin α -MoO₃ layer is placed on a thick α -MoO₃ layer to form the homostructure (Fig.1a), or on a thick layer of β -Ga₂O₃ to form the heterostructure (Fig.1b). Parameters θ_1 and θ_2 represent the corresponding twist angles between the thin and thick layers for both structures. Throughout this work, we will consider that the coordinate axes are aligned to the main crystal axes of the top layer; i.e. the x (y,z) axis is fixed to the [100] ([001], [010]) direction of the top α -MoO₃ layer. Particularly, changing the twist angles must be understood as a rotation of the bottom layer with respect to the [100] direction of the α -MoO₃ top layer. Examples of the polaritonic response expected in these systems are shown in Fig.1c-h, where real-space numerical calculations (see Methods) of the polaritonic field $\text{Re}(E_z)$ produced by a point dipole at the top surface of the thin α -MoO₃ layer are displayed, along with its 2D Fast Fourier Transform (2D-FFT) shown in the insets.

For both systems, there exists a specific twist angle θ for which PhPs propagate with a cross-like shape (Fig.1c,f). The observed dual-directional ray-like propagation is clearly distinct from the hyperbolic propagation, where several fringes with a hyperbolic shape propagate far from the source. Yet, mirror symmetry with regard to both [100] and [001] α -MoO₃ crystal axes, typical for polaritonic response in single layers of orthorhombic biaxial materials, is conserved for these cases. We, therefore, term this condition the symmetrical case. Remarkably, these mirror symmetries are broken when considering different twist angles (Fig.1d,e,g,h). In particular, the polariton ray along one direction gradually increases its electromagnetic field intensity and propagates further when varying the twist angle between the layers. For the rays along the other direction, the opposite effect occurs: their intensity is reduced and the rays become shorter until they almost disappear. Through a gradual adjustment of the twist angle, we can maximize both effects. At an optimal twist angle, only one branch gives rise to polariton propagation, while the other branch is suppressed completely (Fig.1e,h). Therefore, unidirectional propagation of PhPs emerges naturally in these systems constituting a perfect platform for the development of applications where a strong directional control of light at the nanoscale is required. Remarkably, the PhPs excited in these extremely anisotropic cases exhibit a ray-like behavior; in other words, the direction of propagation is perpendicular to the wavefronts, which present a constant phase.

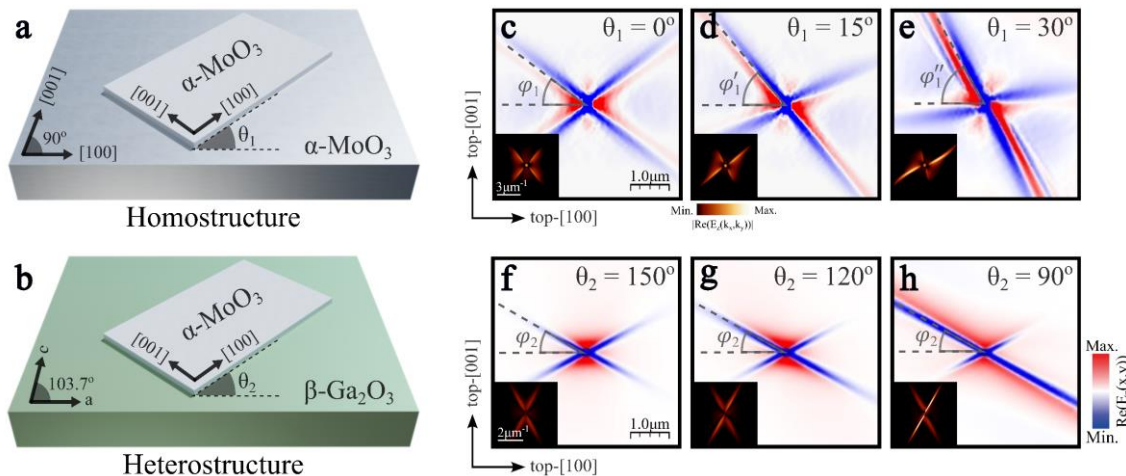


Figure 1: Unidirectional ray polaritons in twisted asymmetric stacks. **a-b.** Schematic of the two systems under study: **a.** 80 nm-thin α -MoO₃ layer placed over a 3 μm -thick α -MoO₃ layer (homostructure) and **b.** 100 nm-thin α -MoO₃ layer on top of a 5 μm -thick β -Ga₂O₃ layer (heterostructure). Parameters θ_1 and θ_2 represent the twist angle of the thick bottom layer with regard to the thin top layer for both systems, respectively. **c-h.** Real-space electric fields $\text{Re}(E_z)$ launched by a point dipole source at the thin α -MoO₃ surface for the homostructure (**c-e**) and the heterostructure (**f-h**) at illumination frequencies $\omega =$

920 cm^{-1} and 734 cm^{-1} , respectively. The twist angles are $\theta_1 = 0^\circ$ (c), 15° (d), 30° (e) and $\theta_2 = 150^\circ$ (f), 120° (g), 90° (h). The in-plane direction of ray-like propagation is marked with dashed grey lines at an angle defined by φ_1 , φ_1' and φ_1'' (c-e) and φ_2 (f-h) with respect to the [100] crystal direction of the top α - MoO_3 layer. The 2D-FFTs of the simulated real-space images are shown in the insets of c-h.

This polariton propagation in real-space corresponds to a linear, unidirectional behavior also in the momentum space representation (insets of Fig.1e,h), where the majority of polariton momentum components point in a single direction. This effect is in stark contrast to previous observations of unidirectional propagation of canalized PhPs in twisted bilayers and trilayers of α - MoO_3 ³⁰⁻³⁴. There, employing twisted thin layers of similar thickness results in linear IFCs that are offset from the origin, and thus contain omnidirectional momentum components. From a fundamental point of view, the unidirectional linear IFCs introduce a variety of unexplored phenomena in which reflection³⁵⁻³⁷ and refraction³⁶⁻⁴⁰ are prominent examples. Notably, the direction of propagation of both rays in the homostructure rotates gradually with the twist angle. This effect becomes clear when extracting the φ_1 value, which represents the direction of the twist-enhanced ray with respect to the [100] top layer direction. We extract $\varphi_1 = 36^\circ$, 50° and 63° from Fig.1c,d,e, respectively. Thus, changing the twist angle between the layers not only enhances the amplitude and propagation length of that ray but also rotates the whole cross by a similar angle.

The behavior of the heterostructure is very similar in general, however, also exhibits some differences. Firstly, the symmetric case (Fig.1f) emerges at a non-trivial twist angle due to the frequency-dependent optical axis direction of β - Ga_2O_3 ²⁴⁻²⁶. Upon twisting (Fig.1g,h), the intensity and propagation length ratio between both ray directions change similar to the homostructure behavior. However, and in contrast to the homostructure, the direction of the enhanced ray, defined by φ_2 , remains constant independent of the twist angle of the thick β - Ga_2O_3 layer. Consequently, although both asymmetric structures support unidirectional polariton rays, there are also distinct differences in their behavior, suggesting that the physical reason for unidirectional ray propagation may be different. Hence, the two structures constitute an ideal platform for the study of the complex generation of PhPs in twisted bilayer systems with vastly different layer thicknesses.

Unidirectional ray polaritons in twisted homostructures

To demonstrate experimentally the existence of URPs in twisted homostructures, we first fabricated a stack formed by a thin α - MoO_3 layer ($d_{top} = 80$ nm) over a thick α - MoO_3 layer ($d_{bot} = 3$ μm) with twist angles $\theta = 30^\circ$ and 60° (see Methods). The propagation of PhPs (launched with the help of a 200-nm diameter hole fabricated by focused ion beam milling) was visualized by scattering-type scanning near-field optical microscopy (s-SNOM, see Methods). The image obtained for the case of $\theta = 30^\circ$ and $\omega = 880$ cm^{-1} (Fig.2a) shows a bright polaritonic fringe that propagates decaying in amplitude from the hole along the in-plane direction defined by $\varphi = 30^\circ$. Parallel to this fringe, a second dark fringe is formed, revealing that the polaritonic wavefront is completely perpendicular to the 30° direction of propagation. This observation constitutes, as previously described, the fingerprint of unidirectional ray-like propagation. To further corroborate this result, we perform a 2D-FFT on the experimental image. The resulting IFC (inset in Fig.2a) shows a linear shape, demonstrating the existence of only one allowed direction for both the polaritonic wavevector and the energy flow (perpendicular to the wavevector), as expected for a ray.

To investigate the spectral response and potential tunability of URPs in the twisted homostructure, we measured other illumination frequencies within the [100] hyperbolic α - MoO_3 Reststrahlen band¹⁴⁻¹⁷, as shown in Fig.2b,c for $\omega = 900$ cm^{-1} and 920 cm^{-1} , respectively (see SI.2 for other different frequencies). The experimental images obtained show unidirectional ray-like propagation of PhPs similar to Fig.2a; however, the direction of the ray varies with frequency. In fact, as illustrated in the s-SNOM images (dashed lines), the angle between the direction of propagation of the PhPs and the [100] top layer direction, φ , undergoes a change of up to 30° between $\omega = 880$ cm^{-1} and $\omega = 920$ cm^{-1} . This effect can also be

appreciated by observing the evolution with frequency of the slope of the linear IFCs in the FFT. This frequency behavior enables unprecedented control over light propagation at the nanoscale. Despite numerous studies in twistoptics successfully demonstrating control over the directionality of light and the polaritonic response³⁰⁻³⁴, a common challenge across these works stems from the need for mechanical twist angle variation between layers. Here instead, we demonstrate that the orientation of the PhP propagation can be actively tuned by simply changing the excitation frequency. Consequently, twisted asymmetric homostructures serve as ideal platforms for a range of potential applications, including routers or directional biosensors.

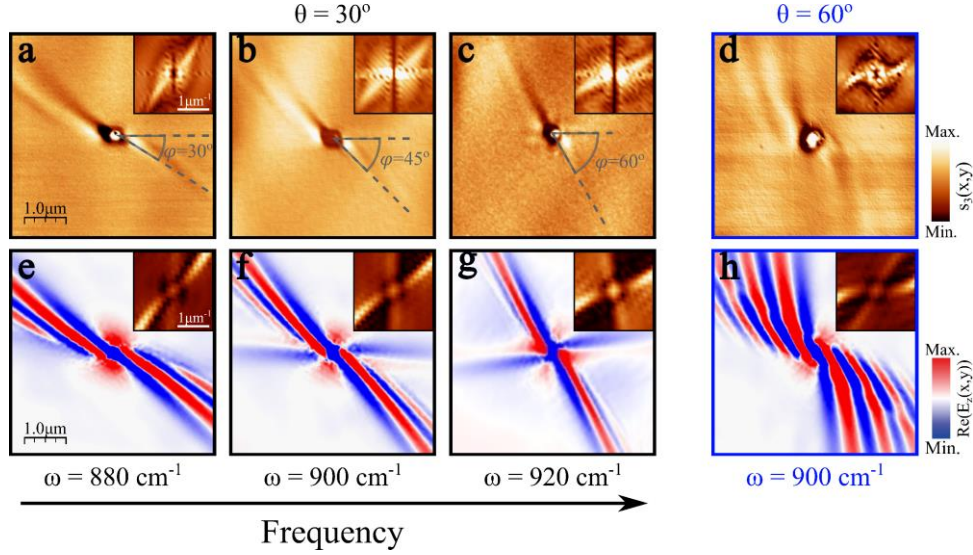


Figure 2: Observation of unidirectional ray polaritons in twisted asymmetric homostructures. **a-d.** Near-field amplitude image in a twisted structure made of a thin α -MoO₃ layer ($d_{top} = 80$ nm) over a thick α -MoO₃ layer ($d_{bot} = 3$ μ m) with twist angles $\theta = 30^\circ$ (**a-c**) and 60° (**d**) at an illuminating frequency of $\omega = 880$ cm^{-1} , 900 cm^{-1} , 920 cm^{-1} and 900 cm^{-1} for **a-d**, respectively. A 200-nm diameter hole allows efficient launching of the PhPs, whose wavefronts and direction of propagation are visualized by s-SNOM. For **a-c** the in-plane direction of propagation is marked with grey lines at an angle defined by φ with respect to the [100] crystal direction of the top α -MoO₃ layer. The experimental IFCs (2D-FFT of the near-field image) are shown in the insets, verifying polariton unidirectional propagation in the direction defined by φ . **e-h.** Simulated near-field amplitude images of the system in **a** (**e**), **b** (**f**), **c** (**g**) and **d** (**h**). The FFT of the simulated images are shown in the top insets of **e-h**.

To corroborate these experimental results, we performed full-wave numerical simulations (Fig.2e-g), showing excellent agreement with the s-SNOM near-field real-space images, both in terms of the shape of the polariton wavefront and its propagation direction. The simulations, as well as the experiments, are characterized by the presence of a single polariton ray and the almost complete absence of the other one, rendering these polaritons fully unidirectional. The simulations only show a very faint polaritonic feature close to the [100] direction corresponding to a weak polaritonic mode along the second asymptote in the IFC, which is almost completely suppressed (see insets). Twisting the two layers reduces the intensity and increases the losses of one of the previously crossed rays towards its full suppression, enabling URPs. Remarkably, the angular distance between the enhanced and the suppressed ray becomes bigger with frequency. This is in excellent agreement with the frequency evolution of the IFCs for a single thick layer of α -MoO₃ (see SI.3). Careful inspection of the FFTs of the experimental and simulated propagation patterns reveals that the IFCs are not perfectly linear but show a slight curvature. With increasing frequency this curvature of the IFCs diminishes, resulting in a reduced number of fringes (see SI.3).

A more extreme PhP behavior can be observed for a twist angle of $\theta = 60^\circ$ (Fig.2d). An unprecedented “pinwheel” pattern arises naturally from the asymmetric homostructure. Several polariton fringes can be observed within a narrow angular sector. However, for this configuration the phase fronts are curved generating a completely different field profile compared to the URPs observed at the smaller twist angles. Both features can be clearly

identified from the momentum space data (FFT in the inset in Fig.2d). As before, one branch of the IFC is much stronger than the other, resulting in strongly unidirectional propagation, however, with a significant curvature of the IFCs consistent with the emergence of several curved fringes covering a narrow angular sector in real space. Again, the numerical simulation for $\theta = 60^\circ$ (Fig.2h) is in excellent agreement with the experimental result, matching both directionality and periodicity of fringes.

To conceptually understand why URPs emerge in the asymmetric homostructure, we performed numerical simulations (Fig.3) of the transition from a symmetric α -MoO₃ twisted bilayer (equal thicknesses of the layers) to the asymmetric homostructure. For consistency, we nominally maintain the thickness of the top α -MoO₃ layer constant as $d_{top} = 80$ nm, and increase the thickness of the twisted bottom layer: $d_{bot} = 80$ nm, 500 nm and 3 μ m, keeping a twist angle of $\theta = 30^\circ$ and an illumination frequency of $\omega = 900$ cm⁻¹. A scheme of the three structures is shown in Fig.3a-c. For the symmetric bilayer (Fig.3a), a typical hyperbolic PhP propagation³⁰⁻³³, slightly tilted due to the coupling between the two layers, can be observed in the real-space images and the resulting IFCs (Fig.3e,i). Increasing the bottom layer thickness to 500 nm (Fig.3b) results in significant changes in the PhP propagation. Two distinct effects can be identified in the simulated near-field data (Fig.3f); (i) an irregular hyperbolic pattern propagates close to the horizontal direction. Note that the intensity of these fringes decays more quickly than in the symmetric bilayer. (ii) The fringes become longer, slightly curved and more aligned along the diagonal. Both effects maximize for the thickest bottom layer (Fig.3c). Here, the phase fronts flatten out completely and lose their hyperbolic shape. At this point, only the diagonal fringes persist, yet in a much flatter manner, generating the unidirectional ray-like propagation observed in Fig.2b,f.

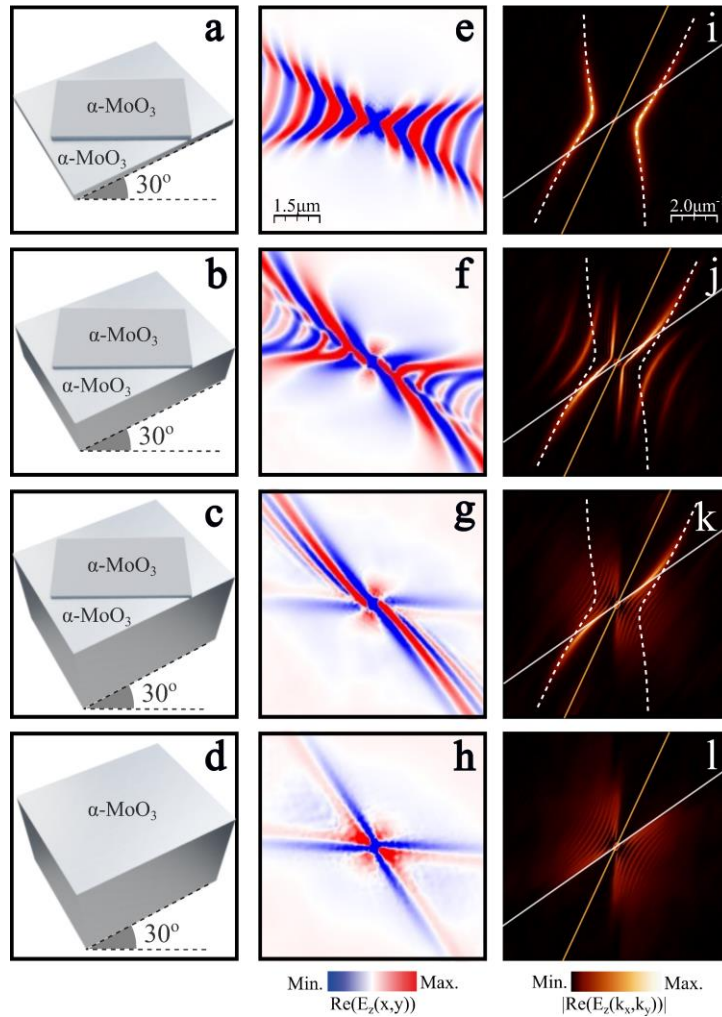


Figure 3: Analysis of the thickness disparity in twisted homostructures. a-d. Schemes of four systems made of α -MoO₃ layers. The top thin layer in a-c has a thickness of $d_{top} = 80$ nm while the bottom has

$d_{bot} = 80$ nm (a), $d_{bot} = 500$ nm (b), $d_{bot} = 3$ μ m (c). Scheme d corresponds to a single thick layer of α -MoO₃ ($d = 3$ μ m). In all cases, the twist angle is $\theta = 30^\circ$ and the illumination frequency is $\omega = 900$ cm⁻¹. e-h. Numerical simulations showing the near-field $\text{Re}(E_z)$ generated by a point dipole located above the four structures represented in a-d, respectively. i-l. IFCs obtained by performing the 2D-FFTs of the near-field images in e-h, respectively. White dash curves in i-k correspond to the analytic IFC of the bilayer case shown in a. White and orange lines in i-l are the asymptotes of the IFCs of PhPs in the bottom and top layers, respectively.

A fundamental explanation of the physical effect responsible for this behavior can be found in the momentum space representation (Fig.3i-l). The white dashed line in Fig.3i-k corresponds to the analytic IFC of the symmetric bilayer obtained with Eq. (S1), previously derived in ref. 34. Remarkably, the IFCs for the thicker bottom layers (Fig.3j,k) converge towards the IFC of the symmetric bilayer for high momentum values at a specific angular region defined by the white and orange lines in the panels. These lines correspond to the asymptotes of the IFC for the bottom and top layers, respectively, when considered alone. They are defined by the angle φ at which the real part of the in-plane projected permittivity:

$$\varepsilon_{MoO_3}^\varphi \equiv \varepsilon_{MoO_3,x} \cos^2 \varphi + \varepsilon_{MoO_3,y} \sin^2 \varphi \quad (1)$$

vanishes, $\Re[\varepsilon_{MoO_3}^\varphi(\varphi)] = 0$. Consequently, in the narrow cone between these two lines, the top layer has negative projected permittivity values whereas $\Re[\varepsilon_{MoO_3}^\varphi(\varphi)] > 0$ for the bottom layer. Therefore, in this angular region the bilayer structure effectively supports a polariton mode confined to the top layer that is modified by a positive permittivity substrate. This holds in particular for large momentum components, where the mode decays rapidly into the bottom layer such that its finite thickness does not contribute (see SI.4). Hence, increasing the substrate thickness has little influence on the IFC at large momentum values. As a result, the IFC of the asymmetric homostructure tends towards the IFC of the symmetric bilayer for large momenta.

On the other hand, the part of the IFC in the symmetric bilayer that is outside the narrow cone between the white and orange lines belongs to the angular sector where the projected permittivity of the bottom layer is negative. This implies that in this momentum range each layer supports polariton modes. Increasing the bottom layer thickness decreases the confinement of the respective modes, which translates into IFCs with smaller momentum values. This feature can be clearly observed at the IFC of the 500 nm-thick bottom layer (Fig.3j). When the bottom layer is sufficiently thick (Fig.3k), the polaritons in the full structure are dominated by the bottom layer modes with low confinement. For this momentum region, the wavelength of the bottom layer polariton approaches the free-space wavelength values and, thus, no interference with the thin top layer is expected. This becomes clear when finally removing the top layer and only considering the thick bottom layer (Fig.3d). The short length-scale propagation pattern of this single thick slab (Fig.3h) also shows a ray-like, yet symmetric, propagation pattern²⁰. The corresponding IFC of this thick layer (Fig.3l) resembles the IFC of the stacked homostructure in this region of momentum space. With all these elements we can understand the dispersion of the asymmetric homostructure as a coupling between two separate modes: the mode of the top layer modified by the positive substrate permittivity of the bottom layer (which remains constant independent of the bottom layer thickness), and a ray-like mode (corresponding to one of the asymptotes in momentum space) of the thick bottom layer. A similar argument can be made to explain the ‘‘pinwheel’’ pattern observed for a twist angle of 60° . In this case, one part of the bilayer IFC (exhibiting a canalized behavior, see SI.5) couples with one asymptote of the thick layer to generate the observed propagation.

Unidirectional ray polaritons in twisted heterostructures

To experimentally demonstrate URPs also in the case of a heterostructure, we fabricated stacks of thin α -MoO₃ layers over a thick (010) β -Ga₂O₃ substrate ($d_{bot} = 500$ μ m) at three different twist angles $\theta = 0^\circ, 45^\circ$ and 70° (see Methods). These angles were estimated by using polarization-resolved Raman spectroscopy (see SI.6). A 1- μ m diameter hole was made on the top layer (see Methods) to efficiently launch PhPs, allowing us to directly image their

propagation using s-SNOM. The lower-energy optical phonon resonances of β -Ga₂O₃ require longer wavelength excitation not readily available from commercially available table-top sources. Instead, a broadly tunable infrared free-electron laser⁴¹⁻⁴⁴ (IR-FEL) coupled to an s-SNOM was employed (see Methods) for near-field imaging of ray polaritons in the twisted heterostructure.

The experimental images for three different twist angles obtained at an illumination frequency of $\omega = 734 \text{ cm}^{-1}$ are shown in Fig.4a-c. A cross-like pattern with the same orientation and open angle appears for the three twist angles. However, the propagation lengths of each ray differ between the three structures. For a twist angle of 0° (Fig.4b), both rays exhibit a similar behavior. In contrast, for $\theta = 45^\circ$ and 100° (Fig.4a,c, respectively) there is a notable asymmetry between them. For $\theta = 45^\circ$ (Fig.4a), one ray extends much further than the other (and further than in the more symmetric case shown in Fig.4b), although both rays can still be clearly resolved. For $\theta = 100^\circ$ (Fig.4c), the directions are flipped, and the other ray shows much longer propagation. The asymmetry is now more pronounced, with the short ray almost completely suppressed. These data provide clear evidence that this asymmetric heterostructure can support URPs. The asymmetric intensity between the rays of each twist angle is strongly supported by the asymmetric intensity distribution of the cross-like shape observed in the momentum-space representation (insets in Fig.4a-c) obtained by performing the 2D-FFT of the experimental images. Notably, the propagation lengths of unidirectional rays in the heterostructure are significantly longer ($> 12 \mu\text{m}$) than what we observed for the homostructure (Fig.2), largely due to the different frequency range and, in consequence, different hyperbolic band of MoO₃ in which this PhP is excited.

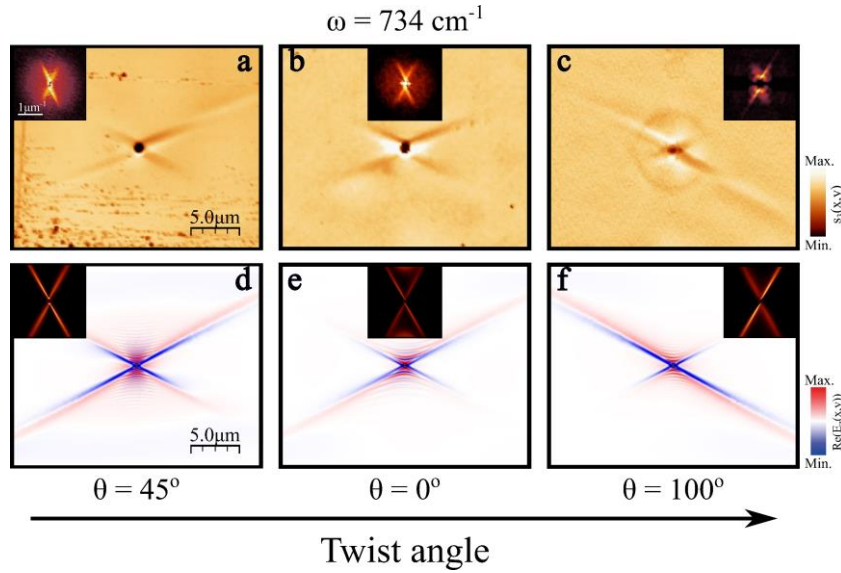


Figure 4: Observation of unidirectional ray polaritons in twisted asymmetric heterostructures. a-c. Near-field amplitude image in a twisted heterostructure formed by a thin α -MoO₃ layer with thicknesses $d_{top} = 200 \text{ nm}$ (a,c) and 400 nm (b) on top of a thick (010) β -Ga₂O₃ substrate ($d_{bot} = 500 \mu\text{m}$) with twist angles $\theta = 45^\circ$ (a), 0° (b) and 100° (c) at an illuminating frequency of $\omega = 734 \text{ cm}^{-1}$. A $1\text{-}\mu\text{m}$ diameter hole allows for effective launching of the PhPs, whose propagation is visualized by s-SNOM. The experimental IFCs (2D-FFT of the near-field image) are shown in the insets. d-f. Simulated near-field amplitude images of the system in a (d), b (e), and c (f). The FFTs of the simulated images are again shown in the insets. Both experimental and simulated images are aligned with the crystallographic axis of the top α -MoO₃ layer.

To corroborate the experimental results, we again performed full-field numerical simulations, as depicted in Fig.4d-f (see Methods for details), which show a remarkable agreement with the experimental real-space images. Note that the shape, the direction of propagation, and the asymmetry between the rays align well with the experimental data. Interestingly, the numerical simulations, in contrast to the experimental images, show hyperbolic-like propagation along the [001] α -MoO₃ axis with a considerably reduced wavelength ($\sim 300 \text{ nm}$). Waves of such small wavelengths, associated with high-order modes of the system, cannot be efficiently excited by

the 1- μm hole in the experiments. Consequently, only ray-like PhPs signatures appear in the experimental data. A similar behavior occurs for different illumination frequencies (see SI.7). However, the asymmetry between the rays varies with frequency for a given twist angle, mainly due to the frequency-dependent rotation of the $\beta\text{-Ga}_2\text{O}_3$ optical axis associated with the shear effect recently reported in this monoclinic crystal²⁴⁻²⁶.

The direction of propagation of ray-like PhPs in the heterostructure remains unchanged independent of the $\beta\text{-Ga}_2\text{O}_3$ twist angle, as observed in Fig. 4. In fact, this direction coincides with the asymptotes for PhPs of the $\alpha\text{-MoO}_3$ top layer, which are defined by Eq. (1). For $\omega = 734 \text{ cm}^{-1}$ this equation gives rise to an in-plane angle of $\pm 61^\circ$ with respect to the $[100]$ crystal direction of the top $\alpha\text{-MoO}_3$ layer, in the momentum space representation, corresponding to a real space propagation direction of $\mp 29^\circ$. Although these angles align well with the direction of propagation observed in the experimental images, high losses are expected for PhPs whose propagation is dominated by the IFC asymptotes of the $\alpha\text{-MoO}_3$ layer. Consequently, the $\beta\text{-Ga}_2\text{O}_3$ substrate must be the main reason why these asymptotic modes appear while it simultaneously also introduces asymmetry to the PhP dispersion.

Interestingly, a symmetric ray-like propagation effect has also been observed in a single thin $\alpha\text{-MoO}_3$ layer over a SiC substrate²² at an illumination frequency of $\omega = 943 \text{ cm}^{-1}$. This frequency corresponds to the surface dipole excitation of SiC where the real part of the dielectric permittivity takes the value -1 ⁴⁵. At this condition, two PhP rays propagate along the asymptotic $\alpha\text{-MoO}_3$ directions. To corroborate whether a similar effect is happening for our heterostructure, we first simulate the PhP propagation in a thin $\alpha\text{-MoO}_3$ on top of an isotropic substrate with a permittivity value of $\epsilon_{sub} = -1$ at an illumination frequency of $\omega = 734 \text{ cm}^{-1}$ (Fig.5a). As in ref. 22, a cross-like pattern arises for this artificial system. In this context, it is useful to analyze the permittivity of the $\beta\text{-Ga}_2\text{O}_3$ substrate at this frequency. Indeed, $\beta\text{-Ga}_2\text{O}_3$ supports in-plane hyperbolic PhPs at $\omega = 734 \text{ cm}^{-1}$, with the real part of the projected permittivity ϵ_{bGO}^φ ranging from $4 \gtrsim \text{Re}(\epsilon_{bGO}^\varphi) \gtrsim -1$. In particular, there is a single in-plane angle φ_c for which a similar condition ($\epsilon_{sub} = -1$) appears. Specifically, $\epsilon_{bGO}^{\varphi_c} = -0.94 + 0.11i$ and $\epsilon_{bGO}^z = -0.95 + 0.03i$ for $\varphi_c = 33^\circ$ with respect to the $\beta\text{-Ga}_2\text{O}_3$ a-axis direction. Thus, a unique condition arises when this specific direction of the $\beta\text{-Ga}_2\text{O}_3$ substrate aligns with the $\alpha\text{-MoO}_3$ asymptotes at certain twist angles, which is largely responsible for the formation of the URPs that we observe.

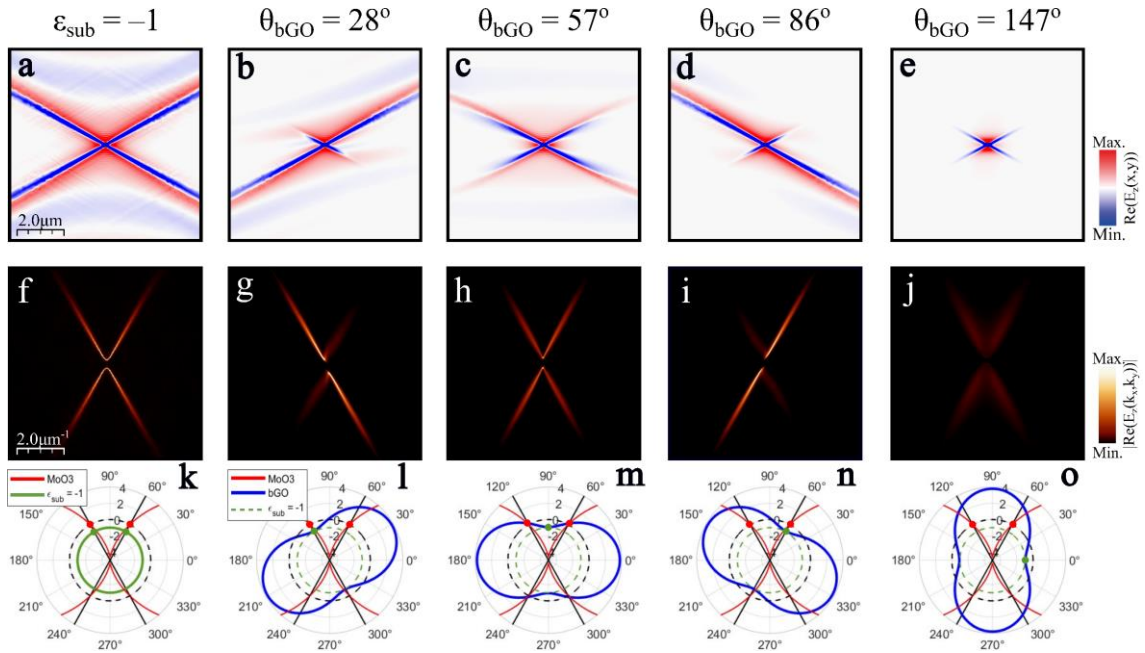


Figure 5: Analysis of the ray asymmetry in twisted asymmetric heterostructures. a-e. Simulated near-field amplitude images of a system made of a 100 nm $\alpha\text{-MoO}_3$ layer over an isotropic substrate with permittivity $\epsilon_{sub} = -1$ (a), and over a thick $\beta\text{-Ga}_2\text{O}_3$ substrate ($d_{bot} = 5 \mu\text{m}$) with twist angles $\theta = 28^\circ$ (b), 57° (c), 86° (d) and 147° (e). The illumination frequency is $\omega = 734 \text{ cm}^{-1}$. **f-j.** Simulated IFCs of **a-e**

obtained by performing the 2D-FFTs of the simulated near-field images **a-e**, respectively. **k-o**. In-plane real permittivity values of α -MoO₃ (red curve), an isotropic material with permittivity $\epsilon_{sub} = -1$ (green curve) and β -Ga₂O₃ (blue curve). The black straight lines represent the two angular directions of the α -MoO₃ asymptotes which are defined by a zero-permittivity α -MoO₃ value (red spots). The permittivity value of -1 for β -Ga₂O₃ is marked by a green spot. When the green and red spots are aligned, unidirectional ray-like propagation occurs along the corresponding asymptote. The black dashed curve corresponds to the value $\epsilon = 0$ and is present for visual guidance.

To corroborate this interpretation, we calculated the near-field response of the heterostructure at several twist angles $\theta = 28^\circ, 57^\circ, 86^\circ$, and 147° , see Fig.5b-e, respectively, along with the respective FFTs shown in Fig.5g-j. By choosing these specific values, we align the unique direction ϕ_c of the β -Ga₂O₃ substrate from being along and in between, the α -MoO₃ asymptotes. Clearly, extreme asymmetry with almost entirely unidirectional ray-like propagation is achieved if ϕ_c is aligned with either asymptote of the α -MoO₃ layer, while symmetric rays emerge for ϕ_c aligned between the asymptotes. Notably, the unidirectional rays propagate significantly further than the symmetric ones, further corroborating the enhancement of ray-like propagation at the approximate $\epsilon_{sub} = -1$ condition. The relative alignment of the projected permittivities of both materials for each twist angle are detailed in Fig.5l-o. Additionally, the green dots mark the ϕ_c direction of the β -Ga₂O₃ substrate, and the red dots mark the direction of the asymptotes of the α -MoO₃ layer, graphically illustrating the alignment of the critical directions of both materials in the twisted heterostructure. For the anisotropic cases, Fig.5l,n, the suppressed rays emerge at directions where the substrate projected permittivity is positive ($\epsilon_{bGO}^p = 2.5 + 1.5i$ and $\epsilon_{bGO}^p = 2.5 + 2i$ for Fig.5l,n, respectively), which is responsible for suppressing the propagation. Note that the imaginary part of these values is different due to the shear effect recently demonstrated in this monoclinic material²⁴⁻²⁶. This suppression of either ray for the asymmetric patterns is consistent with strong suppression of both rays at $\theta = 147^\circ$ (Fig. 5e,j,o) where the substrate projected permittivity is positive and large along both asymptotes, while at $\theta = 57^\circ$ (Fig.5c,h,m) the substrate permittivity takes values near zero along the asymptotes resulting in intermediate propagation lengths for both rays. The gradual suppression of polariton propagation for directions away from ϕ_c condition is related not only to the real part but also to the imaginary part of the projected substrate permittivity (see SI for details), modifying not only confinement but also optical losses for the polaritons through twisting the heterostructure layers. Thus, the β -Ga₂O₃ substrate offers an anisotropic permittivity able to support the asymptotic polariton propagation in the α -MoO₃ layer within a narrow angular region. By twisting the heterostructure we can select the degree of asymmetry between the two α -MoO₃ asymptotes, allowing for the generation of URPs whose direction is locked to the asymptotes of the α -MoO₃ layer.

Our analysis shows that the physical reason responsible for the appearance of URPs is the alignment of the negative β -Ga₂O₃ radial permittivity values with the α -MoO₃ asymptotes. In contrast, the shear effect associated with the monoclinic β -Ga₂O₃ does not play a major role for the unidirectional ray formation. However, there are some features which cannot be understood without considering this shear effect. (i) The slight asymmetry between the two rays in the symmetric cases (Fig.5c,h,m and Fig.5e,j,o) is caused by the asymmetric imaginary response of β -Ga₂O₃ (see SI.11). (ii) The optimal twist angle for which unidirectional ray-like PhPs arise varies with frequency. Apart from the frequency dependence of the α -MoO₃ PhP asymptote directions, also the optical axis direction in β -Ga₂O₃ changes with frequency, leading to a nontrivial evolution of ray-like PhPs with frequency (see SI for more details).

Discussion

The two asymmetric structures considered in this work have been found to both support URPs with a high degree of tunability and unique properties. On the one hand, the direction of URPs in the homostructure, formed by two α -MoO₃ layers, can be modified by simply varying the excitation frequency. On the other hand, in the twisted heterostructure formed by a thin α -MoO₃ layer and a thick β -Ga₂O₃ substrate, the asymmetry of the two rays can be tuned by means of both twist angle and illumination frequency variations. We explain the PhP response in the

homostructure as the result of the coupling of two separate modes: a mode of the top thin α -MoO₃ layer modified by the positive bottom layer permittivity and a ray-like mode of the bottom thick α -MoO₃ layer. This is the reason why modifying the twist angle changes dramatically the PhP response, i.e., from unidirectional ray-like PhPs to “pinwheel” shaped PhPs. In contrast, the URPs in the heterostructure follow a different mechanism. At a given frequency, the narrow angular sector of negative projected permittivity of the β -Ga₂O₃ substrate enhances PhP rays if twist-aligned with the asymptotes of the α -MoO₃ layer. By twisting the structure, we can control the degree of asymmetry between the two rays. The monoclinic nature of β -Ga₂O₃ and the associated shear effects play a minor role, and the polariton features emerge solely from its in-plane anisotropy. Interestingly, the URPs observed in this work are characterized by a propagation at constant phase along a direction of effective zero permittivity suggesting similarities with epsilon-near-zero physics⁴⁶⁻⁴⁸, such as a constant phase, diffraction-less propagation, yet with extreme intrinsic directionality, leading to a large range of open fundamental questions, as well as unique opportunities for photonic applications that rely on nanoscale waveguiding and routing.

Conclusions

In conclusion, by employing asymmetrically stacked, twisted biaxial crystals we demonstrate the natural emergence of unidirectional ray PhPs. We experimentally visualize these polaritonic excitations in two twisted asymmetric structures involving either a thin and a thick layer of the orthorhombic crystal α -MoO₃, or one thin layer of α -MoO₃ and a thick substrate of the monoclinic crystal β -Ga₂O₃. We find that the URPs supported in these structures can be tuned by means of variations of the twist angle and the illumination frequency. These features are crucial for the implementation of twisted asymmetric structures in optical nanotechnologies. In addition, unprecedented PhP propagations, such as pinwheel PhPs, arise naturally from these structures. We theoretically explain the appearance of unidirectional ray propagation in the homo- and heterostructure systems, providing much insight into the complex excitation and propagation of PhPs in twisted systems. In this regard, the large variety of hyperbolic vdW materials, as well as hyperbolic 3D-crystals, opens a plethora of new possibilities for exploring the limits of PhP propagation in twisted multilayers and provides a large material base for nanophotonic applications.

Methods

Fabrication of twisted stacks.

The twisted stacks were fabricated using the dry transfer technique⁴⁹. α -MoO₃ layers were extracted from mechanical exfoliation of commercial α -MoO₃ bulk materials (Alfa Aesar) using Nitto tape (Nitto Denko, SPV 224P). For the homostructure, a thin and a thick α -MoO₃ flake were exfoliated from the Nitto tape to a transparent poly-(dimethylsiloxane) (PDMS) stamp, where selection of the desired thicknesses was carried out using an optical microscope. Subsequently, we employed a home-made micromanipulator for aligning and twisting the PDMS stamps with the α -MoO₃ flakes forming the stack. To do this, we first released the thick α -MoO₃ flake on a SiO₂ substrate by heating the PDMS stamp to 200 °C, and finally, we placed the thin α -MoO₃ flake on top of it while twisting it at the desired angle. For the heterostructure, we used commercially available wafer samples of [010] β -Ga₂O₃ doped with Fe to compensate for inherent free carriers ($\sim 10^{12}$ cm⁻³). We again use the dry transfer technique (following the steps described before) to place several twisted thin α -MoO₃ layers on top of the β -Ga₂O₃ crystal.

Fabrication of the nanoholes.

For the homostructure, the thin α -MoO₃ layers were milled through by FIB processing⁵⁰ using a FEI Helios 600 Nanolab FIB–SEM system. The optimized parameters to produce holes with an average diameter of 224.9 ± 7.6 nm were an ion beam voltage of 30 kV, an ion beam current of 1.5 pA and a dwell time of 2 μ s. The nanoholes of the heterostructure were milled using a FEI Helios NanoLab G3 CX focused ion beam (FIB) with an ion beam voltage of 30 kV and an ion

beam current of 7.7 pA. To remove gallium ion intercalation from both systems, we annealed our samples at 300 °C for 90 minutes in the ambient air.

Scattering-Scanning Near Field Optical Microscopy.

For the homostructure, near-field imaging measurements were performed employing a commercial scattering-type Scanning Near Field Optical Microscope (s-SNOM) from Neaspec GmbH, equipped with a quantum cascade laser from Daylight Solutions (890-1140 cm⁻¹). Metal-coated (Pt/Ir) atomic force microscopy (AFM) tips (ARROW-NCpt-50, Nanoworld) at a tapping frequency $\Omega \sim 280$ kHz and an oscillation amplitude ~ 100 nm were used as source and probe of polaritonic excitations. Both the hole and the AFM tip were illuminated with s-polarized infrared light from the quantum cascade laser. The light scattered by the tip with the near-field information was focused by a parabolic mirror into an infrared detector (Kolmar Technologies) in the far field. Demodulation of the detected signals $n\Omega$, which can be written as the complex-valued functions $\sigma_n = s_n e^{i\phi_n}$, was performed to the 3rd harmonic ($n=3$) of the tip frequency for background suppression. A pseudo-heterodyne interferometric method was employed to independently extract both amplitude (s_3) and phase (ϕ_3) signals.

For the heterostructure, near-field imaging measurements were performed using a commercial s-SNOM system from Neaspec, coupled to the free-electron laser FELBE at the Helmholtz-Zentrum Dresden-Rossendorf. Experimental details are equivalent to those in previous works²⁶. In short, by using the FEL as the infrared light source we rely on self-homoddyne measurements rather than pseudo-heterodyne due to the relative instability of the FEL. This results in intermixed amplitude and phase signals.

Full-wave numerical simulations.

The full-wave numerical simulations were performed using the software COMSOL Multiphysics, based on the finite boundary elements method. The structure was composed of 2 semi-infinite media (superstrate and substrate) with a thin and a thick layer in between and a vertically oriented electric dipole on top of the flake acting as a polaritonic launcher. We calculate the vertical component of the electric field $\text{Re}(E_z)$ at 5 nm on top of the uppermost surface of the twisted stacks, which is then subjected to 2D-FFT to extract the simulate PhP IFCs. Momentum axis of the IFCs is defined as $k = \frac{1}{\lambda}$. The dielectric permittivity values for α -MoO₃ (ref.18) and β -Ga₂O₃ (ref.24) are taken from elsewhere.

Acknowledgements

J.A.-C., A.I.F.T.-M., E.T.-G. and G.A.-P. acknowledge support from the Severo Ochoa program of the government of the Principality of Asturias (nos. PA-22-PF-BP21-100, PA-21-PF-BP20-117, PA-23-PF-BP22-046 and PA-20-PF-BP19-053, respectively). J.M.-S. acknowledges financial support from the Ramón y Cajal Program of the Government of Spain and FSE (RYC2018-026196-I), and the project PCI2022-132953 funded by MCIN/AEI/10.13039/501100011033 and the EU “NextGenerationEU/PRTR”. P.A.-G. acknowledges support from the European Research Council under Consolidator grant no. 101044461, TWISTOPTICS and the Spanish Ministry of Science and Innovation (State Plan for Scientific and Technical Research and Innovation grant number PID2022-141304NB-I00). A.Y.N. acknowledges the Spanish Ministry of Science and Innovation (grant PID2020-115221GB-C42) and the Basque Department of Education (grant PIBA-2020-1-0014). L.H. and J.M.D.T. acknowledge financial support by Gobierno de Aragón via grant E13_23R with European Social Funds (Construyendo Europa desde Aragón). LH and JMDT thank the CSIC Interdisciplinary Thematic Platform (PTI) on Quantum Technologies (PTI-QTEP). Authors acknowledge the use of instrumentation as well as the technical advice provided by the National Facility ELECMI ICTS, node «Laboratorio de Microscopias Avanzadas (LMA)» at «Universidad de Zaragoza». Parts of this research were carried out at the ELBE Center for High-Power Radiation Sources at the Helmholtz-Zentrum Dresden-Rossendorf e. V., a member of the Helmholtz Association. M.O., L.M.E., and S.C.K. acknowledge the financial support by the Bundesministerium für Bildung und Forschung (BMBF, Federal Ministry of Education and Research, Germany, Project Grant Nos. 05K19ODB and 05K22ODA) and by the Deutsche Forschungsgemeinschaft (DFG, German Research Foundation) under Germany’s Excellence

Strategy through Würzburg-Dresden Cluster of Excellence on Complexity and Topology in Quantum Matter—ct.qmat (EXC 2147, project-id 390858490). T.G.F. was supported through the National Science Foundation through grant 2236807. S.D. was supported by the Office of Naval Research MURI grant #N0001-23-1-2567. K.D.-G. was supported by the Army Research Office under grant number W911NF-21-1-0119, while J.D.C. was supported by the Office of Naval Research grant #N00014-22-1-2035 and by the Department of Energy—Basic Energy Sciences under Grant number DE-FG02-09ER4655. G.C., N.S.M., S.W., M.W., and A.P. were supported by the Max Planck Society.

Author contributions

J.A.-C., M.O. and S.D. contributed equally to this work. A.I.F.T.-M., E.T.-G. and A.T.M.-L. prepared the twisted α -MoO₃ samples. S.D., A.I.F.T.-M., L.H. and J.M.T. performed the focussed-ion-milling of holes into the α -MoO₃ flakes. T.B. performed Raman measurements to determine the twist angles. J.A.-C., A.I.F.T.-M., E.T.-G., and P.A.-G. carried out the near-field measurements of the α -MoO₃ stacks. M.O., S.D., G.C., G.A.-P., K.D.G., R.K., A.S.S., N.S.M., S.W., J.M.K., T.G.F., J.D.C., and A.P. performed the near-field measurements of the α -MoO₃/ β -Ga₂O₃ stacks. J.A.-C., S.D., C.L., L.F.-A., and A.P. carried out the numerical calculations. M.W., S.C.K., L.M.E., J.M.-S., A.Y.N., J.D.C., and P.A.-G. acquired part of the funding required to carry out this work. J.A.-C., P.A.-G. and A.P. wrote a first version of the manuscript that was edited by the rest of authors. S.C.K., A.Y.N., J.D.C., P.A.-G. and A.P. supervised the work. J.A.-C., P.A.-G., and A.P. conceived the original idea.

References

1. Basov, D. N. et al. Polaritons in van der Waals materials. *Science* **354**, aag1992 (2016).
2. Low, T., Chaves, A., Caldwell, J. et al. Polaritons in layered two-dimensional materials. *Nature Mater* **16**, 182–194 (2017).
3. Caldwell, J. D. et al. Low-loss, infrared and terahertz nanophotonics using surface phonon polaritons. *Nanophotonics* **4**, 44–68 (2015).
4. He, M. et al. Ultrahigh-resolution, label-free hyperlens imaging in the Mid-IR. *Nano Lett.* **21**, 7921–7928 (2021).
5. Autore, M., Li, P., Dolado, I. et al. Boron nitride nanoresonators for phonon-enhanced molecular vibrational spectroscopy at the strong coupling limit. *Light Sci Appl* **7**, 17172 (2018).
6. Bylinkin, A., Schnell, M., Autore, M. et al. Real-space observation of vibrational strong coupling between propagating phonon polaritons and organic molecules. *Nat. Photonics* **15**, 197–202 (2021).
7. Dai, S., Ma, Q., Andersen, T. et al. Subdiffractive focusing and guiding of polaritonic rays in a natural hyperbolic material. *Nat Commun* **6**, 6963 (2015).
8. Li, P., Lewin, M., Kretinin, A. et al. Hyperbolic phonon-polaritons in boron nitride for near-field optical imaging and focusing. *Nat Commun* **6**, 7507 (2015).
9. Dai, S. et al. Internal nanostructure diagnosis with hyperbolic phonon polaritons in hexagonal boron nitride. *Nano Lett.* **18**, 5205–5210 (2018).
10. Biehs, S. A., Tschikin, M., Messina, R. & Ben-Abdallah, P. Super-Planckian near-field thermal emission with phonon-polaritonic hyperbolic metamaterials. *Appl Phys. Lett.* **102**, 131106 (2013).
11. Castilla, S., Vangelidis, I., Pusapati, VV. et al. Plasmonic antenna coupling to hyperbolic phonon-polaritons for sensitive and fast mid-infrared photodetection with graphene. *Nat Commun* **11**, 4872 (2020).
12. Galiffi, E., Carini, G., Ni, X. et al. Extreme light confinement and control in low-symmetry phonon-polaritonic crystals. *Nat Rev Mater* **9**, 9–28 (2024).
13. Dai, S. et al. Tunable Phonon Polaritons in Atomically Thin van der Waals Crystals of Boron Nitride. *Science* **343**, 1125–1129 (2014).
14. Caldwell, J., Kretinin, A., Chen, Y. et al. Sub-diffractive volume-confined polaritons in the natural hyperbolic material hexagonal boron nitride. *Nat Commun* **5**, 5221 (2014).

15. Zheng, Z. et al. Highly confined and tunable hyperbolic phonon polaritons in van der Waals semiconducting transition metal oxides. *Adv. Mater.* **30**, e1705318 (2018).
16. Ma, W., Alonso-González, P., Li, S. et al. In-plane anisotropic and ultra-low-loss polaritons in a natural van der Waals crystal. *Nature* **562**, 557–562 (2018).
17. Zheng, Z. et al. A mid-infrared biaxial hyperbolic van der Waals crystal. *Sci. Adv.* **5**, eaav8690 (2019).
18. Álvarez-Pérez, G. et al. Infrared permittivity of the biaxial van der Waals semiconductor α -MoO₃ from near- and far-field correlative studies. *Adv. Mater.* **32**, 1908176 (2020).
19. Taboada-Gutiérrez, J., Álvarez-Pérez, G., Duan, J. et al. Broad spectral tuning of ultra-low-loss polaritons in a van der Waals crystal by intercalation. *Nat. Mater.* **19**, 964–968 (2020).
20. Voronin, K. et al. Fundamentals of Polaritons in Strongly Anisotropic Thin Crystal Layers. *ACS Photonics* **11**, 550–560 (2024).
21. Ma, W., Hu, G., Hu, D. et al. Ghost hyperbolic surface polaritons in bulk anisotropic crystals. *Nature* **596**, 362–366 (2021).
22. Duan, J. et al. Enabling propagation of anisotropic polaritons along forbidden directions via a topological transition. *Sci. Adv.* **7**, eabf2690 (2021).
23. Hu, G., Ma, W., Hu, D. et al. Real-space nanoimaging of hyperbolic shear polaritons in a monoclinic crystal. *Nat. Nanotechnol.* **18**, 64–70 (2023).
24. Schubert, M. et al. Anisotropy, phonon modes, and free charge carrier parameters in monoclinic β -gallium oxide single crystals. *Phys. Rev. B* **93**, 125209 (2016).
25. Passler, N.C., Ni, X., Hu, G. et al. Hyperbolic shear polaritons in low-symmetry crystals. *Nature* **602**, 595–600 (2022).
26. Matson, J., Wasserroth, S., Ni, X. et al. Controlling the propagation asymmetry of hyperbolic shear polaritons in beta-gallium oxide. *Nat Commun* **14**, 5240 (2023).
27. Hu, C., Sun, T., Zeng, Y. et al. Source-configured symmetry-broken hyperbolic polaritons. *eLight* **3**, 14 (2023).
28. Herzig Sheinflux, H. & Koppens, F. H. The rise of twist-optics. *Nano Lett.* **20**, 6935–6936 (2020).
29. Hu, G., Krasnok, A., Mazon, Y., Qiu, C.-W. & Alù, A. Moiré hyperbolic metasurfaces. *Nano Lett.* **20**, 3217–3224 (2020).
30. Hu, G., Ou, Q., Si, G. et al. Topological polaritons and photonic magic angles in twisted α -MoO₃ bilayers. *Nature* **582**, 209–213 (2020).
31. Chen, M., Lin, X., Dinh, T.H. et al. Configurable phonon polaritons in twisted α -MoO₃. *Nat. Mater.* **19**, 1307–1311 (2020).
32. Duan, J. et al. Twisted nano-optics: manipulating light at the nanoscale with twisted phonon polaritonic slabs. *Nano Lett.* **20**, 5323–5329 (2020).
33. Zheng, Z. et al. Phonon polaritons in twisted double-layers of hyperbolic van der Waals crystals. *Nano Lett.* **20**, 5301–5308 (2020).
34. Duan, J., Álvarez-Pérez, G., Lanza, C. et al. Multiple and spectrally robust photonic magic angles in reconfigurable α -MoO₃ trilayers. *Nat. Mater.* **22**, 867–872 (2023).
35. Álvarez-Pérez, G. et al. Negative reflection of nanoscale-confined polaritons in a low-loss natural medium. *Sci. Adv.* **8**, eabp8486 (2022).
36. Folland, T.G., Fali, A., White, S.T. et al. Reconfigurable infrared hyperbolic metasurfaces using phase change materials. *Nat Commun* **9**, 4371 (2018).
37. Fali, A. et al. Refractive index-based control of hyperbolic phonon-polariton propagation. *Nano Lett.* **19**, 7725–7734 (2019).
38. Duan, J., Álvarez-Pérez, G., Tresguerres-Mata, A.I.F. et al. Planar refraction and lensing of highly confined polaritons in anisotropic media. *Nat Commun* **12**, 4325 (2021).
39. Hu, H. et al. Gate-tunable negative refraction of mid-infrared polaritons. *Science* **379**, 558–561 (2023).
40. Sternbach, A. J. et al. Negative refraction in hyperbolic hetero-bicrystals. *Science* **379**, 555–557 (2023).
41. Kehr, S. C., Döring, J., Gensch, M., Helm, M. & Eng, L. M. FEL-based near-field infrared to THz nanoscopy. *Synchrotron Radiation News*. **30**, 31–35 (2017).

42. de Oliveira, T. V. A. G. et al. Nanoscale-confined terahertz polaritons in a van der Waals crystal. *Adv. Mater.* **33**, 2005777 (2021).
43. Wehmeier, L. et al. Phonon-induced near-field resonances in multiferroic BiFeO₃ thin films at infrared and THz wavelengths. *Appl. Phys. Lett.* **116**, 071103 (2020).
44. Kuschewski, F. et al. Narrow-band near-field nanoscopy in the spectral range from 1.3 to 8.5 THz. *Appl. Phys. Lett.* **108**, 113102 (2016).
45. Adachi, S. (1999). The Reststrahlen Region. In: Optical Properties of Crystalline and Amorphous Semiconductors. *Springer*, Boston, MA.
46. Liberal, I., Engheta, N. Near-zero refractive index photonics. *Nature Photon* **11**, 149–158 (2017).
47. Feng, S. Loss-Induced Omnidirectional Bending to the Normal in ϵ -Near-Zero Metamaterials. *Phys. Rev. Lett.* **108**, 193904 (2012).
48. Gomez-Diaz, J. S., Tymchenko, M., Alù, A. Hyperbolic Plasmons and Topological Transitions Over Uniaxial Metasurfaces. *Phys. Rev. Lett.* **114**, 233901 (2015).
49. Castellanos-Gomez, A. et al. Deterministic transfer of two-dimensional materials by all-dry viscoelastic stamping. *2D Mater.* **1**, 011002 (2014).
50. Höflich, K. et al. Roadmap for focused ion beam technologies. *Appl. Phys. Rev.* **10**, 041311 (2023).